Chapter 8
Stochastic Optimal Control of Seismic Structures with MR Dampers

8.1 Preliminary Remarks

Although the active structural control can attain a desired structural performance, the power supply system for implementing the structural control might suffer from a serious damage when subjected to hazardous dynamic excitations (Patten et al. 1998). Moreover, the entire structural system tends to instability due to the inevitable modeling error, measurement noise, and time delay (Soong 1990). A refined means is to actualize the logical combination between the active and passive control modalities so as to carry out a semiactive structural control. This modality exhibits a less demand of external energy and a low risk of system dynamic instability, which has thus received extensive attention in practice (Chu et al. 2005; Dan et al. 2015).

Owing to the perfect dynamic damping behaviors, the magnetorheological (MR) damper is regarded as one of the most promising control devices for implementing the semiactive structural control (Casciati et al. 2006). It has been an active area of research worldwide in the past two decades. The relevant topics include semiactive control algorithms and strategies (Jansen and Dyke 2000; Yoshioka et al. 2002; Nagarajaiah and Narasimhan 2006; Li et al. 2007; Xu and Guo 2008; Hogsberg 2011), modeling and dynamic performance of MR dampers (Spencer et al. 1997; Yang et al. 2002; Tsang et al. 2006; Boada et al. 2011; Xu et al. 2012; Chae et al. 2013), novel materials and technologies (Carlson and Jolly 2000; Tse and Chang 2004; Jung et al. 2010; Imaduddin et al. 2013), real-time hybrid simulations (Carrion et al. 2009; Cha et al. 2013; Asai et al. 2015), etc; while a few attempts, in the theoretical framework of stochastic optimal control, have been carried out for the design and optimization of MR damped structures. For instance, Dyke et al. proposed a LQG clipped-optimal control strategy implemented by MR dampers for strengthening the seismic safety of structures (Dyke et al. 1996). Ni et al. developed a neural network controller with MR damper, which achieved the similar gain to the LQG clipped-optimal controller (Ni et al. 2002). Ying et al. proposed a non-clipped strategy of semiactive stochastic optimal control for nonlinear structural systems with MR dampers based

Y. Peng and J. Li, *Stochastic Optimal Control of Structures*,
https://doi.org/10.1007/978-981-13-6764-9_8

on the stochastic averaging method and stochastic dynamic programming (Ying et al. 2009). Using the modal-based LQG control algorithm and MR dampers, a smart system design was addressed to enhance the seismic performance of base-isolated buildings (Wang and Dyke 2013).

As a semiactive control device, the MR damper needs accurate dynamic models in the application of civil engineering, so as to online predict the control law, i.e., input current, in each time step in view of the relation between the dynamical model, the expected semiactive control force, and the structural state. However, the dynamic constitutive relation of the magnetorheological fluid arises to be complicated since its mechanical behaviors hinge upon a series of factors such as the magnetic field intensity and the shear rate driven by the damper piston. The complex behaviors of the MR fluid bring a challenging issue for accurate modeling of MR dampers. The dynamic test shows as well that the hysteretic behaviors of MR dampers indeed give rise to significant nonlinearity. Therefore, the accurate, simple, and feasible mechanical models ought to be established so as to fulfill the performance of MR dampers and guarantee the real-time effectiveness of the semiactive control strategy.

In this chapter, the method of stochastic optimal control using MR dampers is first introduced. Dynamic modeling, input current identification, and microstructured suspension behaviors of the MR damper are then addressed. For illustrative purposes, the semiactive stochastic optimal control of an MR damped structural system subjected to random seismic ground motion is carried out.

8.2 Semiactive Stochastic Optimal Control Using MR Dampers

A lot of semiactive control algorithms and control strategies have been developed in recent years to fulfill the dynamic performance of MR dampers. For instance, Jansen and Dyke investigated the effectiveness of classical semiactive control algorithms including the Lyapunov stability theory, the LQG clipped-optimal control, the decentralized Bang–Bang control, the modulated homogenous friction, and the maximum energy dissipation (Jansen and Dyke 2000). Chae et al. proposed an updated Maxwell nonlinear slider model for predicting the two-state control modalities of MR dampers subjected to random displacements, i.e., Passive-off and Passive-on, and the variant current and damper outputs (Chae et al. 2013). A semiactive stochastic optimal control in the theoretical framework of the physically based stochastic optimal control was developed (Peng et al. 2017). In conjunction with the bound Hrovat algorithm, the proposed strategy of semiactive stochastic optimal control exhibits the benefits of simplicity and effectiveness.

8.2.1 Bound Hrovat Algorithm

For a randomly excited linear structural system attached with MR dampers, the equation of motion is given by

$$\mathbf{M}\ddot{\mathbf{X}}(t) + \mathbf{C}\dot{\mathbf{X}}(t) + \mathbf{K}\mathbf{X}(t) = \mathbf{B}_s\mathbf{U}_s(t) + \mathbf{D}_s\mathbf{F}(\boldsymbol{\Theta}, t) \tag{8.2.1}$$

where $\mathbf{M}, \mathbf{C}, \mathbf{K}$ are $n \times n$ mass, damping, and stiffness matrices, respectively; $\mathbf{X}$ is the n-dimensional column vector denoting system displacement; $\mathbf{B}_s$ is the $n \times r$ matrix denoting the location of MR dampers; $\mathbf{U}_s$ is the r-dimensional column vector denoting control forces pertaining to MR dampers; $\mathbf{D}_s$ is the $n \times p$ matrix denoting the location of external random excitations; and $\mathbf{F}$ is the p-dimensional column vector denoting random excitation.

The control force of MR dampers typically consists of two parts: the passive damping force that cannot be regulated by the control law and the variable damping force that can be regulated by the control law. Considering a shear-valve mode MR damper that is often applied in practice, the term related to the MR damper force in Eq. (8.2.1) can thus be denoted by

$$\mathbf{B}_s\mathbf{U}_s(t) = -\mathbf{B}_s\mathbf{C}_D\dot{\mathbf{X}}(t) - \mathbf{B}_s\mathbf{U}_{dc}(t) \tag{8.2.2}$$

where $\mathbf{B}_s\mathbf{C}_D\dot{\mathbf{X}}(t)$ denotes the passive damping force and $\mathbf{B}_s\mathbf{U}_{dc}(t)$ denotes the variable Coulombic force which can be regulated through changing the input current and the associated magnetic field intensity which influences the yield strength of the MR fluid. The input current is determined by system state and damper models allowing for implementation of the expected damper force as a certain semiactive control algorithm.

Substituting Eq. (8.2.2) into Eq. (8.2.1), one has

$$\mathbf{M}\ddot{\mathbf{X}}(t) + (\mathbf{C} + \mathbf{B}_s\mathbf{C}_D)\dot{\mathbf{X}}(t) + \mathbf{K}\mathbf{X}(t) = -\mathbf{B}_s\mathbf{U}_{dc}(t) + \mathbf{D}_s\mathbf{F}(\boldsymbol{\Theta}, t) \tag{8.2.3}$$

Introducing the extended state vector $\mathbf{Z}(t) = [\mathbf{X}^{\mathrm{T}}(t)\,\dot{\mathbf{X}}^{\mathrm{T}}(t)]^{\mathrm{T}}$, Eq. (8.2.3) becomes

$$\dot{\mathbf{Z}}(t) = \mathbf{A}\mathbf{Z}(t) + \mathbf{B}\mathbf{U}_{dc}(t) + \mathbf{D}\mathbf{F}(\boldsymbol{\Theta}, t) \tag{8.2.4}$$

where $\mathbf{A}$ is the $2n \times 2n$ system matrix; $\mathbf{B}$ is the $2n \times r$ matrix denoting the location of MR dampers; and $\mathbf{D}$ is the $2n \times p$ matrix denoting the location of random excitation:

$$\mathbf{A} = \begin{bmatrix} \mathbf{0} & \mathbf{I} \\ -\mathbf{M}^{-1}\mathbf{K} & -\mathbf{M}^{-1}(\mathbf{C} + \mathbf{B}_s\mathbf{C}_D) \end{bmatrix}, \mathbf{B} = \begin{bmatrix} \mathbf{0} \\ -\mathbf{M}^{-1}\mathbf{B}_s \end{bmatrix}, \mathbf{D} = \begin{bmatrix} \mathbf{0} \\ \mathbf{M}^{-1}\mathbf{D}_s \end{bmatrix} \tag{8.2.5}$$

In order to attain a good agreement with the dynamic behaviors of MR damper, a simple and efficient control strategy based on the Hrovat algorithm (Hrovat et al.

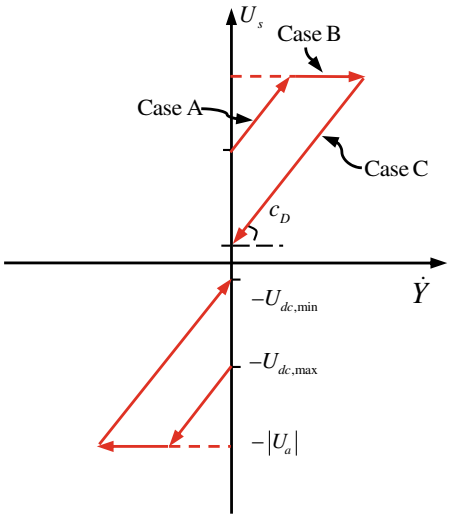

Fig. 8.1 Relation between MR damping force and damper velocity at a certain instant of time in the case of a sample excitation

1983) is developed for the MR damper control, of which the component formulation is given by

$$U_s(\boldsymbol{\Theta},t)=\begin{cases} c_D\dot{Y}(\boldsymbol{\Theta},t)+U_{dc,\max}\operatorname{sgn}(\dot{Y}(\boldsymbol{\Theta},t)), & \text{Case A: } U_a\dot{Y}<0 \text{ and } |U_a|>U_{d,\max} \\ |U_a|\operatorname{sgn}(\dot{Y}(\boldsymbol{\Theta},t)), & \text{Case B: } U_a\dot{Y}<0 \text{ and } |U_a|<U_{d,\max} \\ c_D\dot{Y}(\boldsymbol{\Theta},t)+U_{dc,\min}\operatorname{sgn}(\dot{Y}(\boldsymbol{\Theta},t)), & \text{Case C: } U_a\dot{Y}>0 \end{cases} \tag{8.2.6}$$

where $U_s(\boldsymbol{\Theta},t)$ denotes the semiactive stochastic optimal control force executed by the MR damper; $U_a(\boldsymbol{\Theta},t)$ denotes the reference active stochastic optimal control force; $U_{d,\max}(\boldsymbol{\Theta},t)=c_D\left|\dot{Y}(\boldsymbol{\Theta},t)\right|+U_{dc,\max}$ denotes the changeable maximum damping force of MR damper; $U_{dc,\max}$, $U_{dc,\min}$ denote the maximum and minimum Coulombic forces of MR damper; c_D denotes the viscous damping coefficient of MR damper; and $\dot{Y}(\boldsymbol{\Theta},t)$ denotes the damper velocity, i.e., the motion velocity of piston relative to the damper cylinder which is opposite to the interstory drift between the stories with the MR damper. In these parameters, $U_{dc,\max}$, $U_{dc,\min}$, c_D are the design parameters pertaining to the MR damper.

Figure 8.1 shows the relation between the MR damper force $U_s(\boldsymbol{\theta},t)$ and damper velocity $\dot{Y}(\boldsymbol{\theta},t)$ at a certain instant of time in the case of a sample excitation $\boldsymbol{\theta}$. The control force represented by Eq. (8.2.6) can be realized through driving the calculated current into the MR damper. The expected input current is typically an inverse solution of MR damper models. In application, the control effectiveness of MR dampers highly hinges upon the accuracy and computational cost of the inverse solution. Herein, the input current is assumed to fully implement the control gain in demand with Eq. (8.2.6).

Substituting the formulation of control force as shown in Eq. (8.2.6) into the equation of motion of stochastic dynamical system; say Eq. (8.2.4), one can attain

the solutions of the state vector and the control force. Clearly, the quantities of concern including the component of story velocity $\dot{X}(\boldsymbol{\Theta},t)$, the component of semiactive stochastic optimal control force $U_s(\boldsymbol{\Theta}, t)$, and the active stochastic optimal control force $U_a(\boldsymbol{\Theta}, t)$ are functions of $\boldsymbol{\Theta}$. Similar to Eqs. (3.2.4) and (3.2.5), these quantities satisfy with the generalized probability density evolution equations (GDEEs), respectively, as follows:

$$\frac{\partial p_{\dot{X}\boldsymbol{\Theta}}(\dot{x},\boldsymbol{\theta},t)}{\partial t}+\ddot{X}(\boldsymbol{\theta},t)\frac{\partial p_{\dot{X}\boldsymbol{\Theta}}(\dot{x},\boldsymbol{\theta},t)}{\partial \dot{x}}=0 \tag{8.2.7}$$

$$\frac{\partial p_{U_s\boldsymbol{\Theta}}(u_s,\boldsymbol{\theta},t)}{\partial t}+\dot{U}_s(\boldsymbol{\theta},t)\frac{\partial p_{U_s\boldsymbol{\Theta}}(u_s,\boldsymbol{\theta},t)}{\partial u_s}=0 \tag{8.2.8}$$

$$\frac{\partial p_{U_a\boldsymbol{\Theta}}(u_a,\boldsymbol{\theta},t)}{\partial t}+\dot{U}_a(\boldsymbol{\theta},t)\frac{\partial p_{U_a\boldsymbol{\Theta}}(u_a,\boldsymbol{\theta},t)}{\partial u_a}=0 \tag{8.2.9}$$

Under the provided initial conditions

$$p_{\dot{X}\boldsymbol{\Theta}}(\dot{x},\boldsymbol{\theta},t)|_{t=0}=\delta(\dot{x}-\dot{x}_0)p_{\boldsymbol{\Theta}}(\boldsymbol{\theta}) \tag{8.2.10}$$

$$p_{U_s\boldsymbol{\Theta}}(u_s,\boldsymbol{\theta},t)|_{t=0}=\delta(u_s-u_{s0})p_{\boldsymbol{\Theta}}(\boldsymbol{\theta}) \tag{8.2.11}$$

$$p_{U_a\boldsymbol{\Theta}}(u_a,\boldsymbol{\theta},t)|_{t=0}=\delta(u_a-u_{a0})p_{\boldsymbol{\Theta}}(\boldsymbol{\theta}) \tag{8.2.12}$$

one can attain the probability density functions of the quantities of concern at any instant of time as follows:

$$p_{\dot{X}}(\dot{x},t)=\int_{\Omega_{\boldsymbol{\Theta}}} p_{\dot{X}\boldsymbol{\Theta}}(\dot{x},\boldsymbol{\theta},t)\mathrm{d}\boldsymbol{\theta} \tag{8.2.13}$$

$$p_{U_s}(u_s,t)=\int_{\Omega_{\boldsymbol{\Theta}}} p_{U_s\boldsymbol{\Theta}}(u_s,\boldsymbol{\theta},t)\mathrm{d}\boldsymbol{\theta} \tag{8.2.14}$$

$$p_{U_a}(u_a,t)=\int_{\Omega_{\boldsymbol{\Theta}}} p_{U_a\boldsymbol{\Theta}}(u_a,\boldsymbol{\theta},t)\mathrm{d}\boldsymbol{\theta} \tag{8.2.15}$$

where $\dot{x}_0$, u_{s0}, u_{a0} denotes the initial deterministic values of $\dot{X}(t)$, $U_s(t)$, $U_a(t)$.

8.2.2 Parameter Design of MR Damper

In order to gain a similar control effectiveness as the reference active stochastic optimal control, an MR damper design can be proceeded to facilitate the semiactive

control system. The design principle lies in that the maximum output of the MR damper including the viscous damping force equals to the maximum active optimal control force, i.e., the extreme value of active optimal control force.

Assume that the MR damper control and the active optimal control have a similar control effectiveness, for instance, a same interstory velocity at the moment of the maximum active optimal control force:

$$U_{s,\max}(\boldsymbol{\Theta}) = c_D\left|\dot{Y}_{s|U_{s,\max}(\boldsymbol{\Theta})}\right| + |U_{dc,\max}| = c_D\left|\dot{Y}_{a|U_{a,\max}(\boldsymbol{\Theta})}\right| + |U_{dc,\max}| = U_{a,\max}(\boldsymbol{\Theta}) \tag{8.2.16}$$

Since the output of the MR damper can be continuously tuned by the current-driven magnetic field, there is

$$U_{s,\max}(\boldsymbol{\Theta}) = c_D\left|\dot{Y}_{s|U_{s,\max}(\boldsymbol{\Theta})}\right| + U_{dc,\max} = s\left(c_D\left|\dot{Y}_{s|U_{s,\max}(\boldsymbol{\Theta})}\right| + U_{dc,\min}\right) \tag{8.2.17}$$

where s denotes the tunable times of damper force.

Assuming that the minimum Coulombic force $U_{dc,\min} = 0$, then one has

$$U_{s,\max}(\boldsymbol{\Theta}) = sc_D\left|\dot{Y}_{a|U_{a,\max}(\boldsymbol{\Theta})}\right| = U_{a,\max}(\boldsymbol{\Theta}) \tag{8.2.18}$$

The viscous damping coefficient is thus denoted by

$$c_D = \frac{U_{a,\max}(\boldsymbol{\Theta})}{s\left|\dot{Y}_{a|U_{a,\max}}(\boldsymbol{\Theta})\right|} \tag{8.2.19}$$

and the maximum Coulombic force can be derived from Eqs. (8.2.17) to (8.2.19)

$$U_{dc,\max} = (s-1)c_D\left|\dot{Y}_{a|U_{a,\max}(\boldsymbol{\Theta})}\right| \tag{8.2.20}$$

It is shown in Eq. (8.2.20) that owing to the randomness inherent in the external excitation, the system state and the associated optimal control force are random processes. In this context, the parameters of control law exhibit uncertainties due to the dispersion over the sampling space. For example, the design parameters $U_{dc,\max}$, c_D both rely upon $\boldsymbol{\Theta}$. However, the parameter design and optimization of control law is a deterministic scheme, i.e., the design parameters of structural control ought to be constant regardless of samples of random excitations.

It is revealed that the first step of MR damper control of structures in practice is to gain the expected damper force for the response reduction of structures, and then calculate the input current according to the dynamic model of MR dampers and the real-time system state, i.e., the so-called control law for regulation of MR dampers. In this process, the desired structural performance controlled by the semiactive modality can be precisely derived in theory if the real output of MR dampers just relies upon the amplitude of input current and the real-time state of structural system. This situation, however, is retained under two provided conditions: (i) no measurement noise during

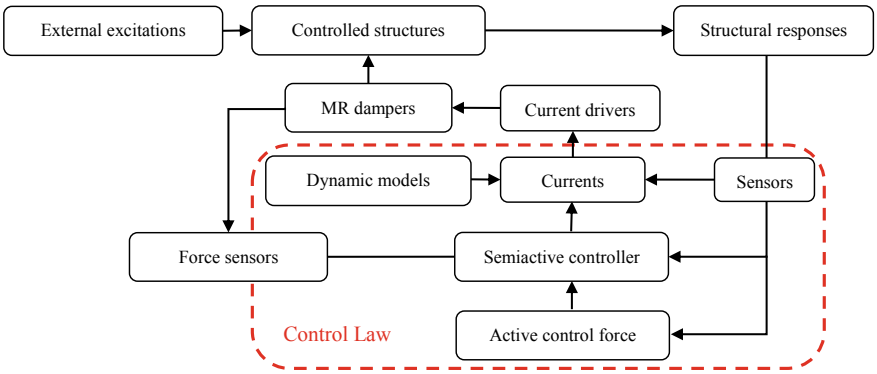

Fig. 8.2 Flowchart of implementing MR damper control of structures

the structural state monitoring and no errors inherent in the current calculation and signal delivery to the damper; (ii) no time delays at each step from state measurement, semiactive control force analysis, input current calculation, and signal delivery to the MR damper. However, there still exist differences between the output of MR damper and the expected semiactive optimal control force even the provided conditions are satisfied, due to the physical constraints of MR dampers such as the complicated rheological behaviors of MR fluids. In fact, the MR damping system belongs to a family of feedback control systems in logic. The associated measurement noise and time delay would exist in the control system. Moreover, the calculated current might exhibit a large diverse from the expected due to the modeling error of MR damper. Therefore, a set of measure system is often used in practice to monitor the real-time output of MR damper, thereby a current compensation strategy is thus proposed to better the control effectiveness of MR damper.

The flowchart of implementing the MR damper control of structures is shown in Fig. 8.2. It is seen that the active control force-based semiactive controller design and the dynamic modeling of MR dampers underly the design and optimization of control law of semiactive control.

8.3 Dynamic Modeling of MR Dampers

8.3.1 Parameterized Model

The dynamic models of MR dampers are mainly classified into parameterized and nonparameterized models (Yang et al. 2013). The parameterized models are mostly the mathematical formulation of damper force derived from the fitted curves of relationships between the damper force and damper displacement or velocity, of which the data is collected from the performance test of MR dampers. The parameterized

models usually consist of a collection of mechanical elements such as the spring element, the viscous damping element, and the Coulomb friction element in configuration of serial and parallel systems (Spencer et al. 1997). The widely used parameterized models of MR dampers are mainly the Bingham model, Gamota-Filisko model, nonlinear bi-viscous hysteretic model, Bouc–Wen hysteretic model, their modified versions, etc. Similarly, the nonparameterized models are derived from the data of performance test of MR dampers, and are formulated by the intelligent algorithms such as neural network and fuzzy logic (Chang and Roschke 1998; Xu and Guo 2008), while these two families of modelings both are built toward the phenomenology and match with the accurate description of macroscale dynamic behaviors of MR dampers. However, the parameterized models exhibit a more feasible extension and a better applicability in practice.

Among the parameterized models, the modified Bouc–Wen hysteretic model is a preferable formulation for dynamic modeling of MR dampers since it not only reveals the hysteretic behavior inherent in the relation between damper force and velocity but also improves the slipperiness of piecewise functional curves. This model was first proposed by Bouc (1967), and later modified by Wen (1976). It has been widely used in modeling of hysteretic structural systems owing to its simplicity and feasibility. However, the Bouc–Wen hysteretic model cannot simulate the roll-off characteristics in the relation curves between damper force and velocity in the case that the acceleration and velocity turn direction and the velocity amplitude are very low. For this reason, a modified Bouc–Wen hysteretic model was then developed by Spencer et al. (1997). The schematic of a shear-valve mode MR damper and its modified Bouc–Wen hysteretic model are shown in Fig. 8.3.

The modified version consists of an original Bouc–Wen hysteretic model in series of a damping element and then in parallel of a spring element, which has the formulation with respect to the output of MR dampers as follows:

$$F_D = c_1\dot{y} + k_1(x - x_0) \tag{8.3.1}$$

$$\dot{y} = \frac{1}{c_0 + c_1}[\alpha z + k_0(x - y) + c_0\dot{x}] \tag{8.3.2}$$

$$\dot{z} = -\gamma|\dot{x} - \dot{y}|z|z|^{n-1} - \beta(\dot{x} - \dot{y})|z|^n + A(\dot{x} - \dot{y}) \tag{8.3.3}$$

where F_D denotes the damper force; $\dot{y}$ denotes the piston velocity; z denotes the hysteretic component; k_1 denotes the equivalent axial spring stiffness of accumulators; c_0 denotes the viscous damping coefficient of MR dampers in the case of large damper velocity; c_1 denotes the damping coefficient of MR dampers in the case of small damper velocity; k_0 denotes the axial stiffness of MR dampers in the case of high damper velocity; x_0 denotes the initial displacement of accumulator spring k_1; α denotes a stiffness parameter defined by the control current and the MR fluid; and γ, β, and A are defined to govern the smoothing of damper force–velocity curves.

For illustrative purposes, the dynamic modeling of MR dampers using the experimental data is carried out, which was derived from a dynamic test of MR damper with

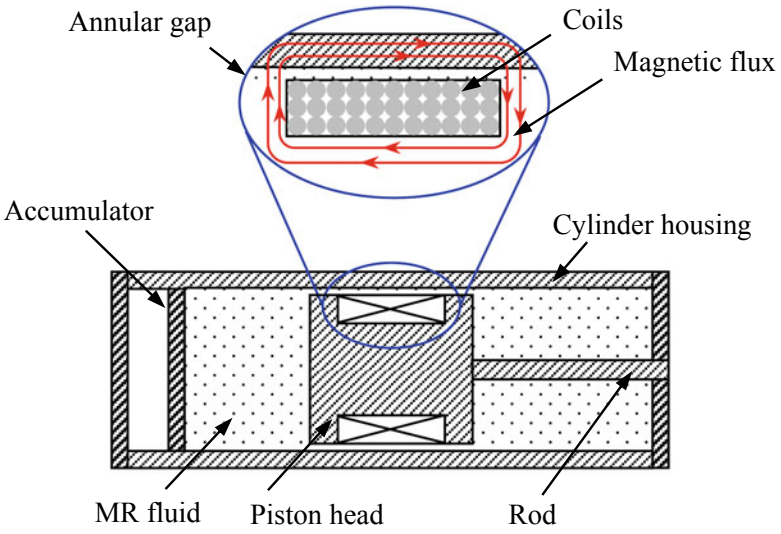

(a) schematic of shear-valve mode MR damper

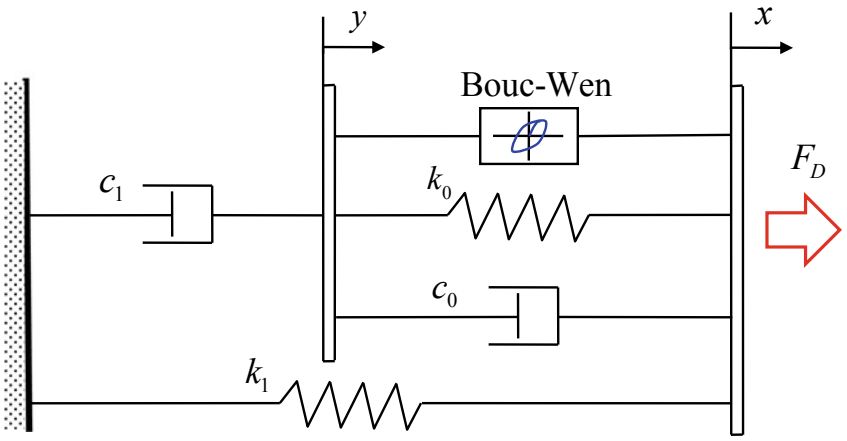

(b) schematic of modified Bouc–Wen hysteretic model

Fig. 8.3 Schematic of shear-valve mode MR damper and its modified Bouc–Wen hysteretic model

specification MRD-100-10 (Peng et al. 2018). The specimens of the MR damper are shown in Fig. 8.4. The two specimens are labeled by MRD-A and MRD-B, respectively. This specification of MR dampers consists of cylinder, piston, MR fluid, and coils, which is a typical single-rod damper, as shown in Fig. 8.3. When the piston moves back and forth relative to the cylinder, the MR fluid passes through the annual gap between the piston and the cylinder, and yields damping force. The damping force can be readily regulated by changing the density of magnetic flux circumfused

around the coils, which is able to be carried out using varying currents driven into MR dampers. The design parameters of the MR damper are listed as follows: maximum output 10 kN, the outer diameter of cylinder 100 mm, the fabrication length 670 mm, the length of stroke ±55 mm, the rated current 2.0 A, and the energy consumption 20 W.

The dynamic test was carried out on an electrohydraulic and servo-controlled material testing machine; see Fig. 8.5. During the test, the active clamp drives the motion of the piston of MR damper so that the piston executes a harmonic motion with specified frequency and amplitude relative to the cylinder. The input current to the MR damper, in four different levels 0.0, 0.5, 1.0, and 1.5 A, is implemented by a DC stabilized power supply. The experimental cases with different displacement amplitudes, excitation frequencies and input currents are proceeded to test the dynamic performance of the MR damper. These experimental cases are listed in Table 8.1.

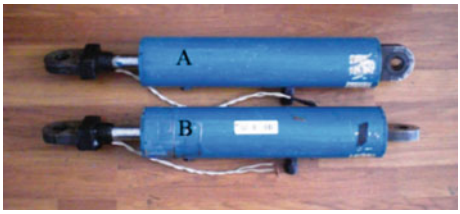

Fig. 8.4 Two specimens of MR damper with specification MRD-100-10

Fig. 8.5 Setup of dynamic test of MR dampers

Table 8.1 Experimental cases of MR damper with specification MRD-100-10

Amplitudes (mm)	Frequencies (Hz)					Currents (A)
	0.25	0.5	0.75	1.0	1.5	
5		√				0.0, 0.5, 1.0, 1.5
10		√				0.0, 0.5, 1.0, 1.5
15	√	√	√	√	√	0.0, 0.5, 1.0, 1.5
20		√				0.0, 0.5, 1.0, 1.5
25		√				0.0, 0.5, 1.0, 1.5

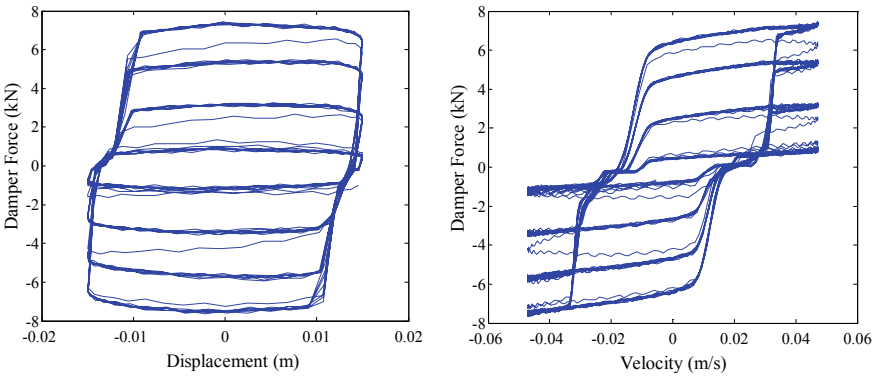

(a) damper force vs. displacement (b) damper force vs. velocity

Fig. 8.6 Testing curves of MRD-A in typical loading conditions with displacement amplitude 15 mm and excitation frequency 0.5 Hz

The testing curves of the MR dampers, i.e., MRD-A and MRD-B, in typical loading conditions with displacement amplitude 15 mm and excitation frequency 0.5 Hz are shown in Figs. 8.6 and 8.7, respectively. Since the input currents are loaded in levels step by step, the curve loops from the inner to the outer are referred to the current level 0.0 A, 0.5 A, 1.0 A, and 1.5 A, respectively. Meanwhile, the relative velocity of the piston of MR damper to the cylinder is calculated through the numerical differential of displacement data monitored in the test.

It is seen that the damper force increases with the enhancement of input current, and the maximum of damper force in each loop arises to be of linear correlation with the input current (the saturation of damper force does not happen since the input current is less than the rated current of MR damper in the experimental cases). In the case of input current 0.0 A, the MR damper possesses viscous behaviors, e.g., the relation curve between damper force and piston displacement approaches to be elliptical, and the relation curve between damper force and piston velocity approaches

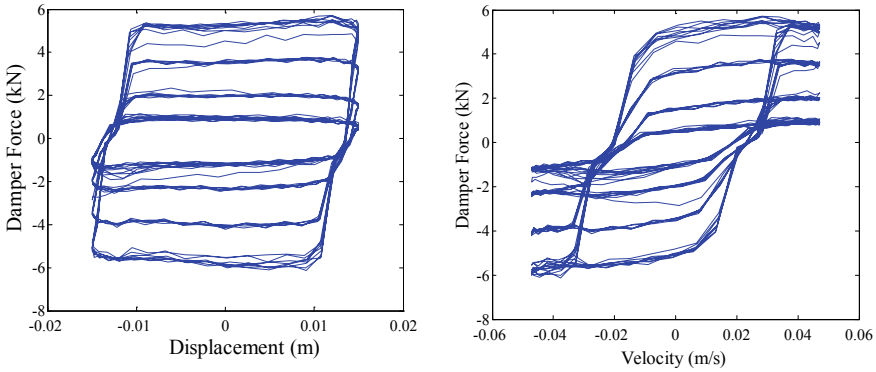

(a) damper force vs. displacement (b) damper force vs. velocity

Fig. 8.7 Testing curves of MRD-B in typical loading conditions with displacement amplitude 15 mm and excitation frequency 0.5 Hz

to be S shape. With the increasing of input current, however, the shear stress of MR fluid becomes stronger as well, thereby the MR damper features a viscous–plastic mechanics. The relation curves between damper force and piston velocity arise to be a complicated hysteretic behavior. In the range of high velocity, the linear relation between damper force and velocity is observed, while in the range of low velocity, a nonlinear relation between damper force and piston velocity is observed where the distinguished hysteretic behaviors occur. These findings are in good agreement with the dynamic model of MR dampers; see Fig. 8.3b.

8.3.2 Parameter Identification of Model

It is seen from Eqs. (8.3.1) to (8.3.3) that the modified Bouc–Wen hysteretic model involves the coupling of differential equations and includes the terms with high orders, which brings about an extremely difficult for the parameter identification of the model. There are three families of schemes for the parameter identification of Bouc–Wen hysteretic models of MR damper. The first refers to traditional optimization methods such as the nonlinear optimization scheme and least squares method with additional constraints (Spencer et al. 1997; Dyke et al. 1998). The second refers to the mathematical analysis of the relation between parameters and forced-limit cycles of model (Ikhouane and Rodellar 2005). The third refers to the genetic algorithm-based parameter identification (Charalampakis and Koumousis 2008). Comparing with the first two families of schemes, the third family of schemes has a better efficiency and accuracy for the optimization of multiple parameters, and is thus applied in this study.

For illustrative purposes, the MR damper MRD-A is considered for the parameter identification of the modified Bouc–Wen hysteretic model. The testing cases of

concern are set as follows: Case 1, loading frequency 0.25 Hz, loading amplitude 15 mm, and loading current 0.0–1.5 A; Case 2, loading frequency 0.50 Hz, loading amplitude 15 mm, and loading current 0.0–1.5 A; and Case 3, loading frequency 1.00 Hz, loading amplitude 15 mm, and loading current 0.0–1.5 A.

Since the modified Bouc–Wen hysteretic model involves the differential equations, a four-order Runge–Kutta method is used to solve the damping force. Meanwhile, a genetic algorithm is employed for parameter identification, which can be readily implemented by the MATLAB toolbox function *ga*. In each step of loop, the assignment and optimization of model parameters are proceeded. The population size, generations, and stall generations in the genetic algorithm toolbox are set as 100, 200, and 50, respectively. The limit of fitness variation between optimized seeds at two neighbor generations is set as 0.001. The solution of differential equations can be derived from the case that all the 10 model parameters are valued through building the logical relation shown in Eqs. (8.3.1)–(8.3.3) with respect to the damper velocity $\dot{y}$ and hysteretic rate $\dot{z}$. For the ready conjunction with the genetic algorithm, nine parameters except the initial displacement x_0 are set as *input*. The input values of the parameters are controlled in real time by the prescribed iterative scheme of genetic algorithm toolbox. The damper force F_D is set as *out*. All the identification values of these parameters are evaluated by the experimental or simulated data. An index pertaining to the degree of fitness is defined as follows (Spencer et al. 1997):

$$Fitness = \frac{\sqrt{\frac{1}{n}\sum_{i=1}^{n}(F_{D,i}^{\exp} - F_{D,i}^{\mathrm{fit}})^2}}{\sqrt{\frac{1}{n}\sum_{i=1}^{n}(F_{D,i}^{\exp} - \frac{1}{n}(\sum_{i=1}^{n}F_{D,i}^{\exp}))^2}} \tag{8.3.4}$$

where n denotes the number of data points in the experiments or simulations; $F_{D,i}^{\exp}$ denotes the damper force of the ith data point; and $F_{D,i}^{\mathrm{fit}}$ denotes the damper force of the ith fitted point.

The modified Bouc–Wen hysteretic model exhibits 10 parameters which might result in a high computational cost and a low accuracy if no constraints are posed upon the parameters. In this study, the initial displacement x_0 of accumulator is set as 0.2 m. The upper and lower bounds of the remaining nine parameters c_1, k_1, c_0, α, k_0, γ, n, β, and A are denoted by $[10^4, 10^7]$, $[10^2, 10^4]$, $[10^2, 10^5]$, $[10^3, 10^5]$, [10, 10^4], $[10^2, 10^5]$, [1, 5], $[10^2, 10^5]$, and [10, 10^3], respectively.

In consideration of the complexity of solving the differential equation, the four-order Runge–Kutta method is implemented by the solver *ode4* of MATLAB/Simulink. The time interval of the solver is fixed at each step so as to derive the damper force at the setting instant of time. In this study, the time interval is set as 0.0001 s, and the time length is set as 20 s.

In the semiactive control modality, an inverse calculation is usually required so as to regulate the damper force through changing the input current or voltage. The analysis of current relevance of model parameters is a critical step, aiming at the determination of sensitive parameters and their functional relation with the input current. The relation curves between parameters and input current reveal that except

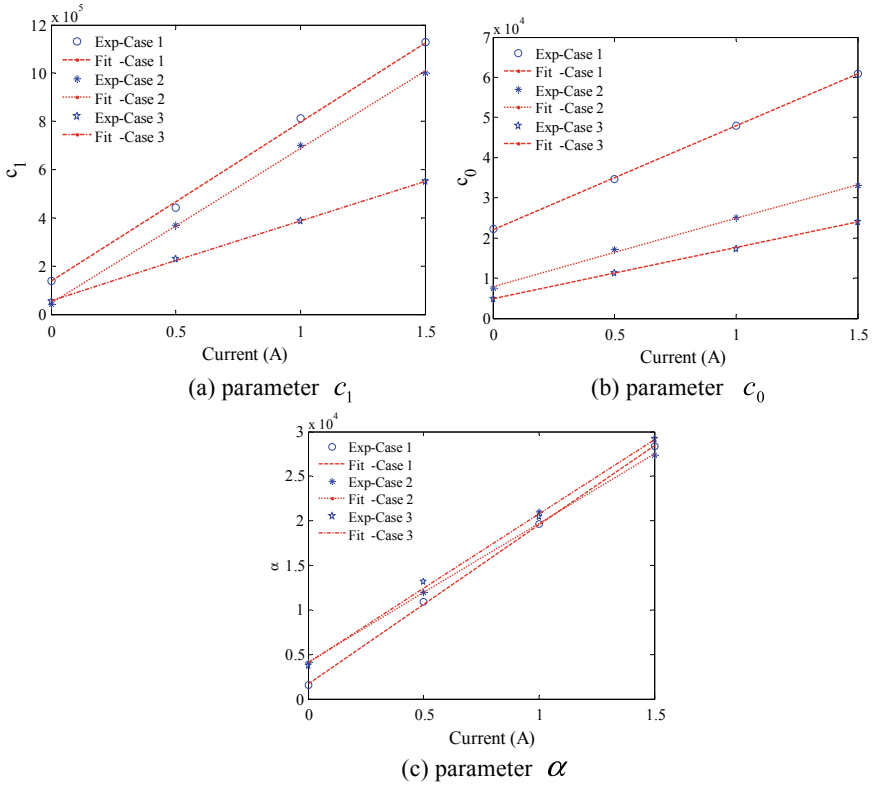

Fig. 8.8 Fitted curves between control parameters and input current

the parameters c_1, c_0, and α, the relation between the remaining six parameters and input current is not clear. The parameters c_1, c_0, and α are the so-called critical parameters for the dynamic model of the MR damper, which change linearly along with the increasing of the current; see Fig. 8.8.

According to Eqs. (8.3.1)–(8.3.3), the identification of the remaining six parameters is carried out again through fixing the functional relation of c_1, c_0, and α with input current. In order to reduce the computational cost, the upper and lower bounds of the parameters to be identified are valued, respectively, by the individual minimum and maximum in the first identification. With an iterative process, the six parameters are eventually defined by Case 1: $[k_1, k_0, \gamma, n, \beta, A] = [782.16, 3007.79, 61530.17, 4.35, 30746.83, 164.20]$, where the fitness is 0.1416; by Case 2: $[k_1, k_0, \gamma, n, \beta, A] = [413.68, 9562.50, 1010.11, 2.00, 1011.73, 105.87]$, where the fitness is 0.1326; and by Case 3: $[k_1, k_0, \gamma, n, \beta, A] = [3609.01, 5012.80, 1944.34, 2.00, 1660.78, 173.43]$, where the fitness is 0.1410.

Using the optimized values of parameters, comparative studies between the modified Bouc–Wen hysteretic model and the experimental data associated with input

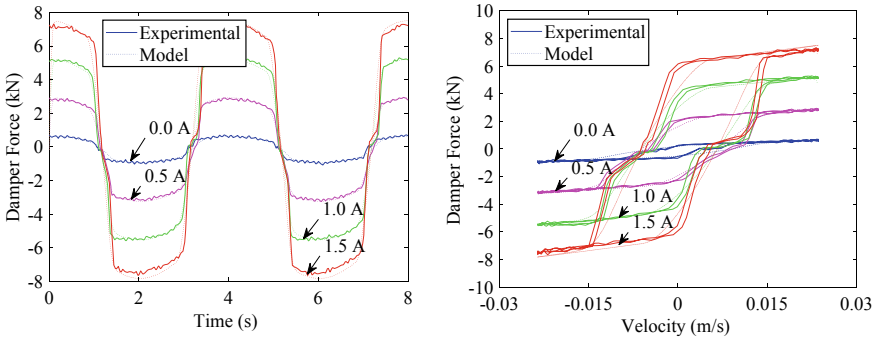

(a) time history of damper force (b) damper force vs. velocity

Fig. 8.9 Comparison between modified Bouc–Wen hysteretic model and experimental data in the case of displacement amplitude 15 mm and excitation frequency 0.25 Hz (Case 1)

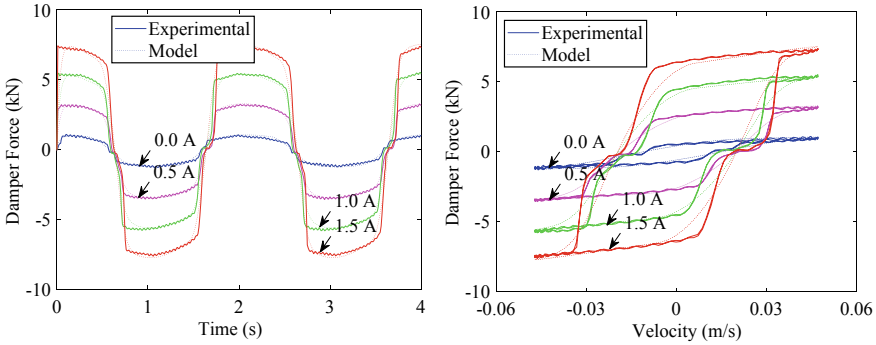

(a) time history of damper force (b) damper force vs. velocity

Fig. 8.10 Comparison between modified Bouc–Wen hysteretic model and experimental data in the case of displacement amplitude 15 mm and excitation frequency 0.50 Hz (Case 2)

currents are proceeded. The model result (labeled as 'Model') and experimental result (labeled as 'Experimental') in the concerned three cases are shown in Figs. 8.9, 8.10 and 8.11, respectively. One might see that the parameterized model secures a sound fitting accuracy with the experimental data in different levels of input current, indicating that identified values of model parameters are satisfied for the individual case. Throughout the three cases, meanwhile, the control parameters, i.e., c_1, c_0, and α, are viewed as the same and all submit to the linear function of input current.

According to the identified model parameters and their relations with the input current, the current signal loaded on the MR damper can be readily generated using the backpropagation (BP) neural network algorithm (Metered et al. 2010). Details of the current signal generation are illustrated in conjunction with the numerical example in Sect. 8.4.

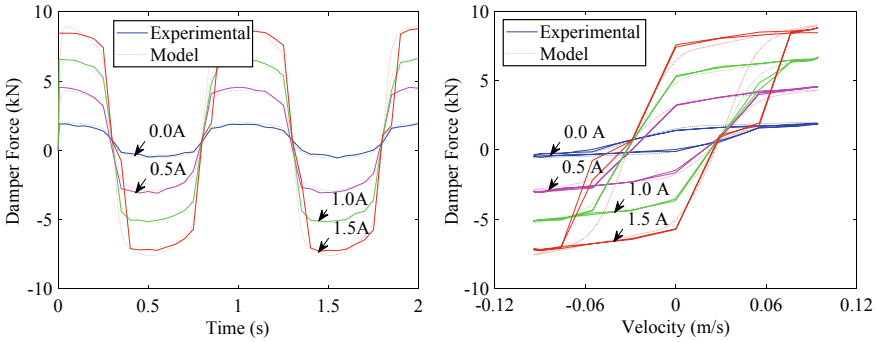

(a) time history of damper force (b) damper force vs. velocity

Fig. 8.11 Comparison between modified Bouc–Wen hysteretic model and experimental data in the case of displacement amplitude 15 mm and excitation frequency 1.00 Hz (Case 3)

8.3.3 Microscale Mechanism of MR Dampers

The investigation of microstructured behaviors of MR suspensions exhibits a significance for revealing the physical essence of complicated dynamics of MR dampers and carrying out the optimization of control law of semiactive modality. The reference (Peng et al. 2012) addressed this issue for the first time.

The magnetorheological fluid is viewed as an elementary material assembling MR dampers. It consists of micrometer-sized magnetizable particles and nonmagnetic fluid, which shows a unique ability to experience the phase separation in a rapid and completely reversible manner. The physical origin of this behavior is that under the external magnetic field with specified intensity, the particles acquire a magnetic dipole moment, resulting in particle aggregation to form chain-like structures parallel to the external magnetic field and form cluster-like and sheet-like structures perpendicular to the external magnetic field. These properties of the phase separation in the microstructure, moreover, are always accompanied by significant changes in flow behavior and optical properties with the increase in the viscosity of the suspension and generation of optical anisotropy. The essence of the MR damper control is thus setting the identified input current as the control law to drive the magnetic field upon the magnetic fluids so that the microstructured behaviors of MR suspensions change and prevent the flow from transporting induced by external excitations. A schematic describing the generation of input current signal and its influence upon the microstructured behaviors of MR suspensions is shown in Fig. 8.12.

A large-scale atomic/molecular massive parallel simulator (LAMMPS) is employed, which provides an embedded routine for large-scale and three-dimensional Brownian dynamics simulation. LAMMPS facilitates the simulations of millions of particles, which may include gas, liquid, solid, and complex phases. Its library of potential functions and force fields is extensive, and it has been applied to the simulation of a wide spectrum of particles, including atomic polymers,

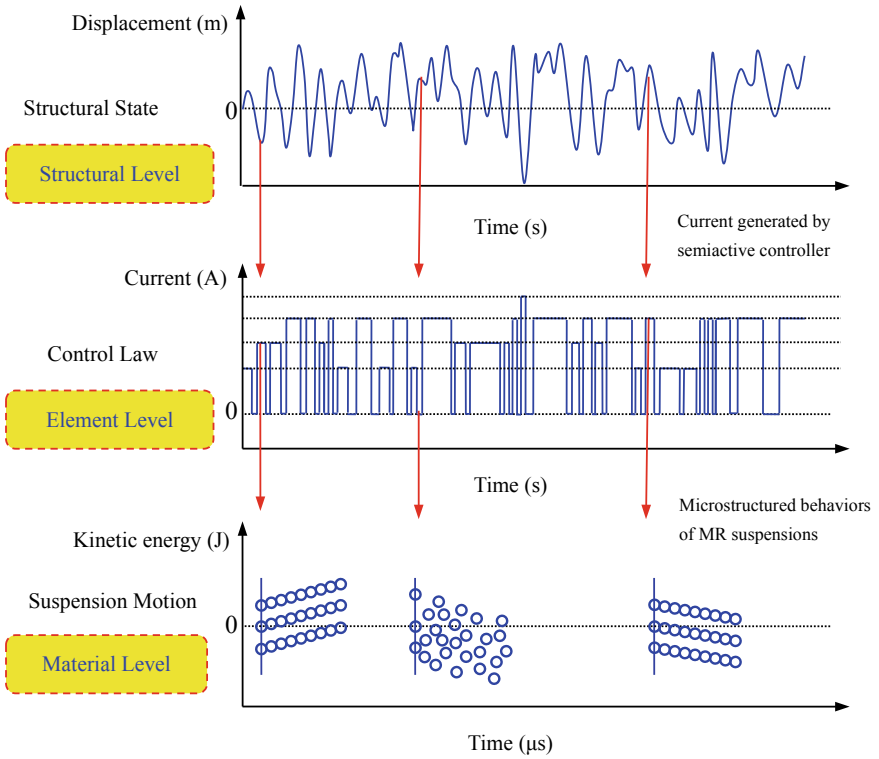

Fig. 8.12 Schematic of input current generation and its influence upon microstructured behaviors of MR suspensions

bead-spring polymers, organic molecules, proteins, granular materials, and point dipolar particles. Moreover, LAMMPS can be readily parallelized for various computer architectures (Plimpton 1995). The initial position and initial velocity of suspensions are generated as statistically independent with a uniform distribution and a Maxwell–Boltzmann distribution, respectively (Liu et al. 2006). The neighbor list algorithm with the strategy of radius cutoff (truncated radius) is used to assess the interaction between particles (Verlet 1967). The motion of MR suspensions can be described by a Langevin equation, of which the numerical solution is derived using the velocity Verlet integral scheme (Swope et al. 1982). These numerical techniques can be readily implemented in conjunction with the LAMMPS.

A shear-valve mode MR damper with double rods in specification of MRD-9000 (Yang 2001) is used for the investigation. The involved MR fluid consists of the silicone oil and the emerged double suspensions with micrometer iron carbonyl particles. The relevant physical parameters of the simulated MR fluid are listed in Table 8.2.

Table 8.2 Physical parameters of simulated MR fluid

Physical quantities		Parameter values
Volume ratio between suspensions and matrix		0.3
Radius of particles	Large particle a_L	5×10^{-6} m
	Small particle a_S	2.5×10^{-6} m
Mass of particles	Large particle M_L	1×10^{-13} kg
	Small particle M_S	1.25×10^{-14} kg
Volume ratio of bidisperse, large/small particles		75:25
Relative permeability	Matrix μ_c	1.0
	Particles μ_p	1×10^3
Saturation magnetization of particles		2 T
Viscosity of matrix		0.3 Pa s
Density of silicon oil		3.6×10^3 kg m^{-3}
Temperature		298 K
Magnitude of steady magnetic field H_0		100 k Am^{-1}

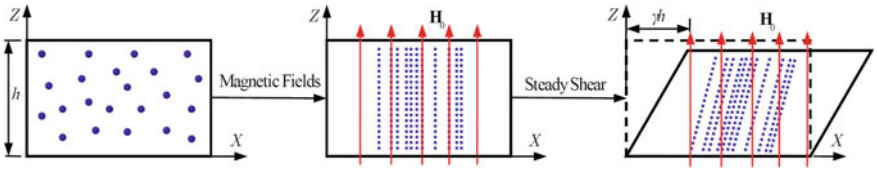

Fig. 8.13 Schematic of magnetic field and steady shear loading on simulated cell

According to the volume ratio between suspensions and carrier fluid, these spheres are uniformly distributed in the space of a simulation cell with dimensions (L_X^*, L_Y^*, L_Z^*) = (20, 10, 10), where the asterisk "*" represents dimensionless quantities. In this study, the length, timescales, and mass in the dimensionless units have specified relation with those in SI units; see dimensionless unit length 10^{-5} m, dimensionless unit time 1.7×10^{-3} s, and dimensionless unit mass 2.43×10^{-8} kg. The amount of particles is 3120 which includes 860 large particles and 2260 small particles. Sheared periodic boundaries are included at $X^* = \pm L_X^*$, $Y^* = \pm L_Y^*$ and $Z^* = \pm L_Z^*$. The shear flow is applied along the X-direction, and the magnetic field is applied along the Z-direction. The time step length of simulations is $\Delta t^* = 10^{-7}$. The schematic of simulation procedure is shown in Fig. 8.13.

Figure 8.14 shows the cluster–sheet phase of the MR suspensions at 10.0 μs, where "o" represents the large particles, and "." represents the small particles. It is seen that the direction of most cluster–sheet structures is parallel to the shorter axis Y, not the longer axis X. In view of the phenomenon of nematic-like ordering of the MR suspensions toward particular directions, one might realize that these magnetic dipoles exhibit some intelligent behaviors, and they always align to clusters along

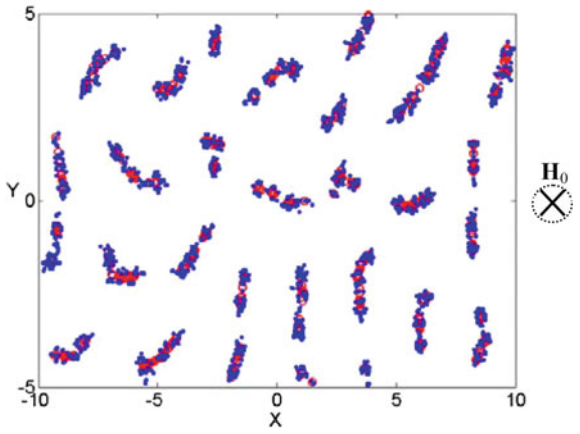

Fig. 8.14 Cluster–sheet phase of MR suspensions at 10.0 μs

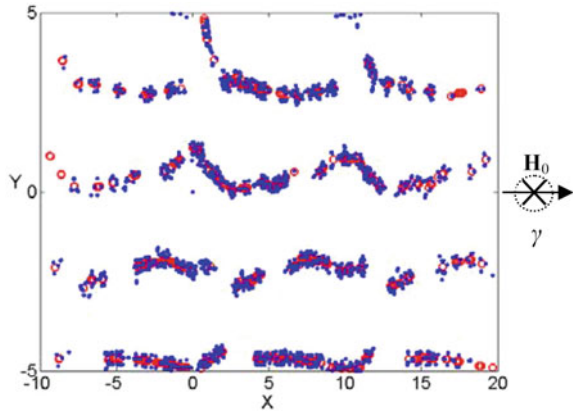

Fig. 8.15 Structural anisotropy of aggregates of MR suspensions at shear strain of 1.0 under steady magnetic field and shear field with shear rate 1000 s^{-1}

the direction whereby the sheet tends to be formed, though the initial configuration admits to the uniform distribution and the external magnetic fields are steady (Peng et al. 2012).

Figure 8.15 shows the structural anisotropy of aggregates of MR suspensions at shear strain of 1.0 under steady magnetic field and shear field with 1000 s^{-1}. It is seen that the suspensions move along the flow field and connect to long sheets along flow direction toward restraining the transportation of the shear flow, though the suspension structure suffers from yielding and the sheets tend to be ripped presenting as arch structures.

In order to reveal the dynamic performance of MR dampers from a microscale, the dynamic yielding stress of MR fluid is simulated. According to the previous studies, the strain energy of macroscale yielding stress of MR fluid in a unit volume equals the kinetic energy of microscale MR suspensions in the volume. On this principle, a multiscale constitutive relation of MR fluids can be established (Peng and Li 2011). Figure 8.16 shows the relation between yielding stress and shear rate of MR fluid

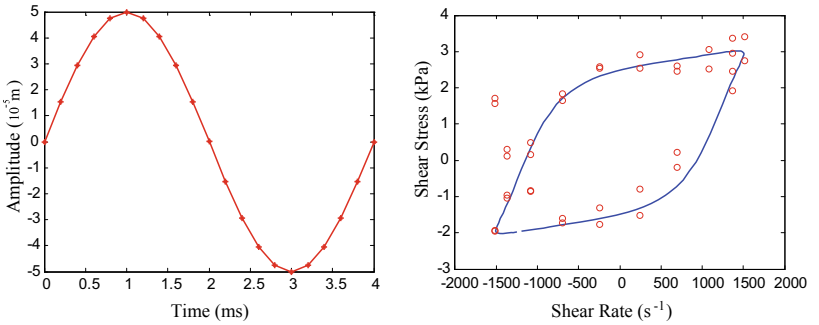

(a) loading path of sine displacement (b) points and fitted curve of yielding stress vs. shear rate

Fig. 8.16 Relation between yielding stress and shear rate of MR fluid under sine displacement loading on MR dampers

under sine displacement loading with period of 4 ms on MR dampers. It is seen that the fitted curve on the simulated data points shows a good consistency with the Bouc–Wen hysteretic model, which exhibits obvious similarities as the relation curves between damper force and damper velocity shown in Figs. 8.10, 8.11 and 8.12. These similarities, as a matter of fact, are just the representation of the macroscale performance of MR dampers under sine displacement loading and current driving on the microscale structured behaviors of MR fluids.

8.4 Numerical Example

The semiactive stochastic optimal control of single-story shear frame shown in Fig. 3.4 is carried out. The physically motivated random seismic ground motion model is used as the external excitation, of which the peak ground acceleration is set as $0.11g$. Design and optimization of a shear-valve mode MR damper are performed for implementing the semiactive control.

In order to attain the desired structural performance, the control algorithm in formulation of Eq. (8.2.6) is employed. The tunable times of the damper force are set as $s = 8$. The design parameters for the MR damper control are viscous damping coefficient and maximum Coulombic force. Since the multilinearity property of the semiactive control algorithm, the original state equation of the structural system shall be discretized into a discrete state equation, and the associated coefficients need to be identified so as to derive the control gain. In this study, the coefficient identification is performed using the precise integration method (Zhong 2004). For the purpose of a uniform numerical framework, the calculation of the reference active optimal control force and its relevant interstory drift refers to the methodology of physically based stochastic optimal control in kernel of discrete dynamic programming, i.e., the solving of a so-called matrix difference Riccati equation; see Appendix E.

The deterministic dynamic analysis with respect to the velocity quantities in the generalized probability density evolution equations employs a first-order forward difference scheme, as same as the discrete dynamic programming. The optimization of weighting matrices in the cost function is carried out as the criterion on system second-order statistics evaluation (SSSE); see Eq. (3.3.21): the interstory drift serves as the constraint, and the quantities of evaluation include the interstory drift, story acceleration, and interstory control force. The quantile function is defined as the sum of mean and three times of standard deviation. The threshold of interstory drift is set as 10 mm.

Since the structural system and seismic ground motion are consistent with the numerical example shown in Sect. 3.4.1, the relation between the statistical moments of equivalent extreme values of system quantities and the ratio of coefficients of weighting matrices, see Fig. 3.11, can be used straightforwardly in this study. In order to reduce the structural displacement in a more serious extent, the weighting matrices pertaining to the system state and control force are denoted by

$$\mathbf{Q_Z} = 80\begin{bmatrix} 1 & 0 \\ 0 & 1 \end{bmatrix}, \mathbf{R_U} = 10^{-12} \tag{8.4.1}$$

By virtue of Eq. (3.3.18), the active stochastic optimal control of structure is proceeded. The probability density function of the extreme value of active optimal control force using the parameters of control law, say Eq. (8.4.1), is shown in Fig. 8.17.

It is seen that the reference active optimal control force exhibits a large range of distribution, of which the mean and standard deviation are 115.44 and 34.68 kN. It is revealed in Eq. (8.2.16) that the parameters of MR dampers are determined by the reference active optimal control force and its relevant interstory velocity. Due to the randomness inherent in the active optimal control force, the parameters of

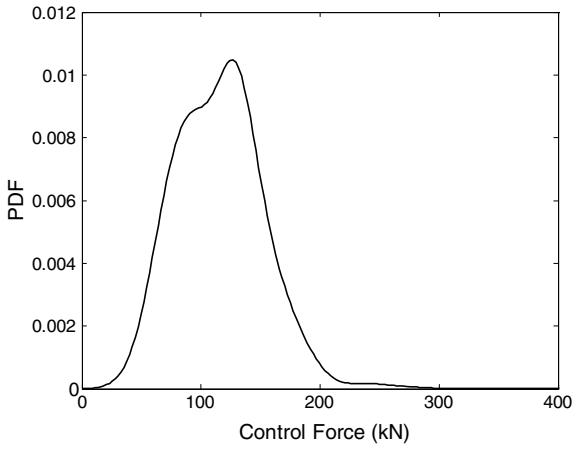

Fig. 8.17 Probability density function of extreme value of active optimal control force

MR damper as the traditional deterministic control scheme give rise to uncertainty. According to the general principle of structural design, the mean or a certain quantile of the active optimal control force can be used as the design control force. One might recognize that this treatment lacks the accurate assessment of structural performance. A logical manner defining the reference active optimal control force is in conjunction with the physical causes.

Figure 8.18 shows the maximum active control force, the maximum interstory drift, and maximum story acceleration of semiactively controlled structure with respect to samples. It is seen that the interstory drift changes not obviously along with the active control force, which nearly distributes in the range of 2–5 mm; the story acceleration changes positively along with the active control force. The tendancy of third-order fitted curves in the figure shows that the application of a larger design active control force cannot attain a further reduction of the structural displacement. It is thus remarked that the semiactive controller and the passive controller lack ability for significantly reducing the structural displacement. However, the active controller exhibits a benefit of reducing the structural displacement. Besides, the fitted curve of relation between story acceleration and active control force has the similarity as that of actively controlled structures.

Figure 8.19 shows the relation between design parameters of MR damper and the active optimal control force with respect to samples. In comparison with Fig. 8.18, it is seen that the viscous damping coefficient is low and insensitive to the active control force when the control force magnitude is more than 100 kN, indicating that an accurate MR damper control system can be constructed using a series of low-cost components; the maximum Coulombic force exposes to be linearly relevant to the reference active control force owing to a linear regulation assumption with respect to the Coulombic force.

In fact, the definition of reference active control force needs to consider the physical mechanism and practical capacity of MR dampers. For example, the most eco-

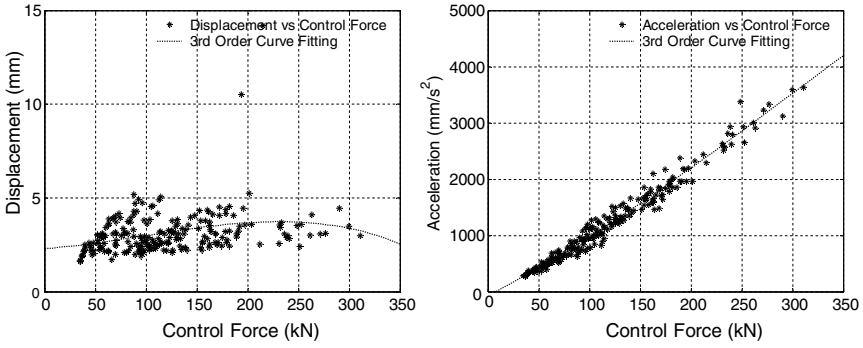

(a) interstory drift vs. active control force (b) story acceleration vs. active control force

Fig. 8.18 Relation between maximum active control force, maximum interstory drift, and maximum story acceleration of semiactively controlled structure with respect to samples

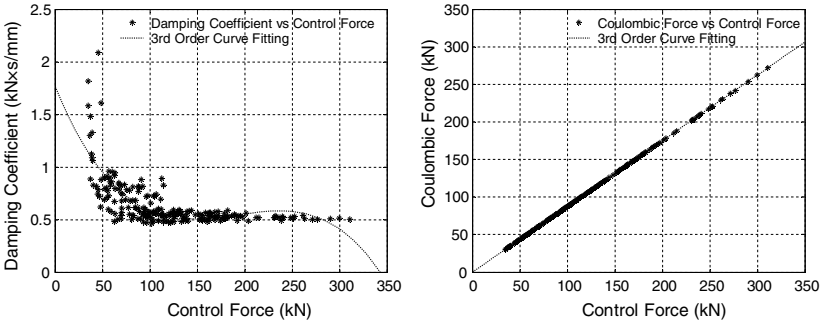

(a) viscous damping coefficient vs. active control force (b) Coulomb force vs. active control force

Fig. 8.19 Relation between maximum active control force, viscous damping coefficient, and maximum Coulombic force with respect to samples

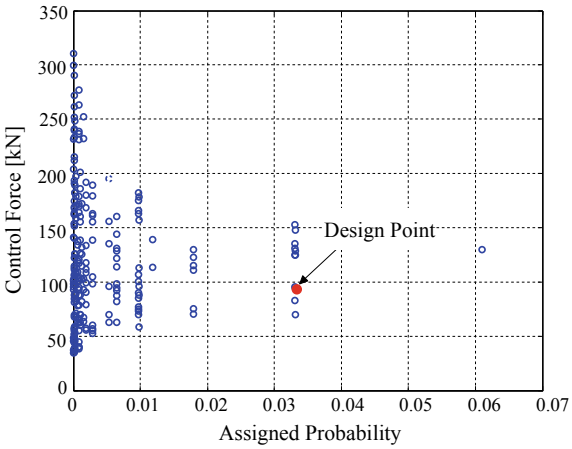

Fig. 8.20 All samples with relation between maximum active control forces and assigned probabilities

nomic output of the MR damper investigated in this study is 200 kN, and a high-viscous rheological liquid is inconvenient for maintenance. Therefore, the reference active control force is suggested to be defined on the sample with the largest assigned probability, i.e., with high occurrence rate, and in the neighborhood of 100 kN. Figure 8.20 shows all the samples with the relation between maximum active control forces and assigned probabilities. It is ready to recognize that the reference active control force is 94.03 kN, which is around the mean of the maximum active control force. The damping coefficient and the maximum Coulombic force are thus designed as 0.6119 kNs/mm, 82.28 kN, respectively.

Time histories of root-mean-square displacement of the structural system with and without controls are shown in Fig. 8.21. It is seen that the structural performance gains a significant improvement both using the semiactive and active stochastic optimal controls. In comparison with the active control, the semiactive control attains an almost same gain in the time domain with smaller response of uncontrolled structure.

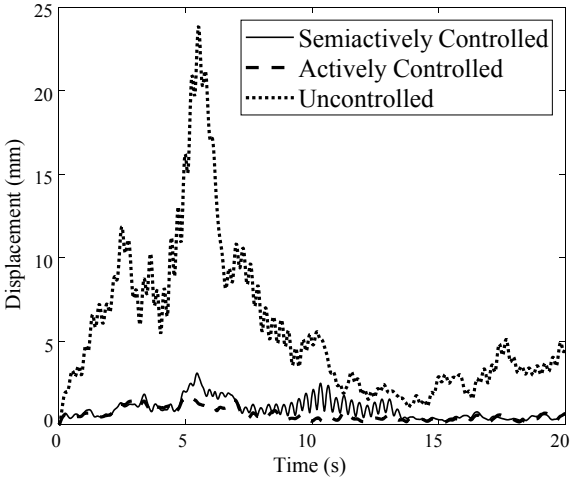

Fig. 8.21 Time histories of root-mean-square displacement of structural system with and without controls

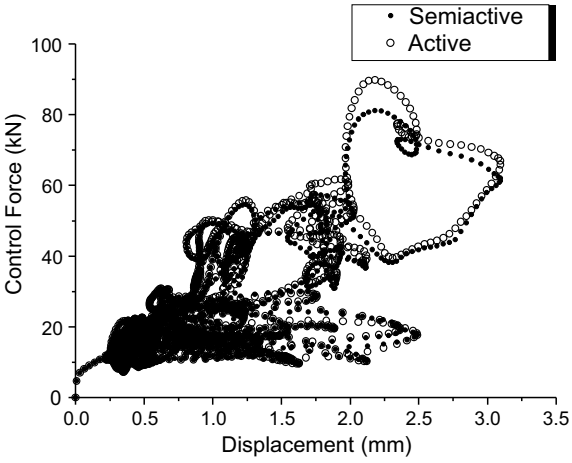

Fig. 8.22 MR damping force tracing active optimal control force in sense of root mean square

In the time domain with larger response of uncontrolled structure, the active control has a better control gain than the semiactive control. This is understood that the semiactive control algorithm employed in this study belongs to a family of bound amplitude control schemes, due to the fact that the MR damper exhibits magnetic saturation (Xu et al. 2012). In the case that the control requirement over the response domain exceeds the capacity of MR damper, the semiactive control will stick on the maximum output of the damper other than timely tracing active optimal control. The detail of MR damper force tracing active optimal control force in root-mean-square sense is shown in Fig. 8.22. It is seen that the bound Hrovat algorithm-based semiactive control has the capacity of tracing the active optimal control in real time.

More accurate probabilistic representation is the probability density function, as shown in Fig. 8.23. It is seen that the curves of PDFs of semiactive and active optimal

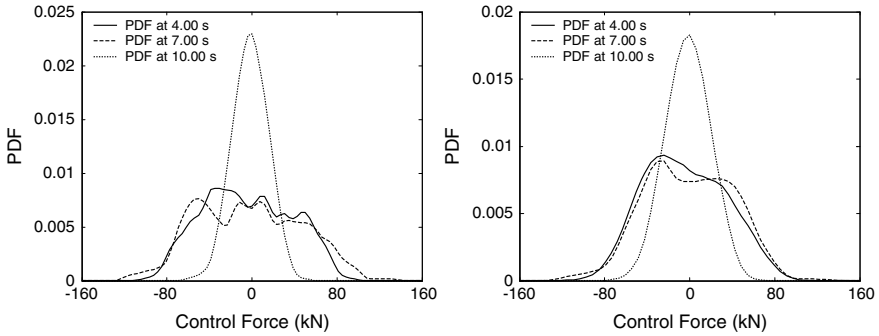

(a) PDFs of semiactive control force (b) PDFs of active optimal control force

Fig. 8.23 PDFs of semiactive and active optimal control forces at typical instants of time

control forces at typical instants of time are similar, where a slight difference lies in that the output of semiactive control merely relies upon the maximum active control force other than tracing the active control force in real time, such as the case that the active control force has a same direction with the interstory velocity or although the active control is opposed to the interstory velocity, the active control force is larger than the maximum output that the MR damper is able to actualize.

Figure 8.24 shows the probability density functions of interstory drift at typical instants of time with and without the MR damper controls. It is seen that the MR damper control can reduce the structural displacement significantly, where the distribution range of PDFs becomes narrower. Meanwhile, by comparison with Fig. 3.13b, the reduction of displacement amplitude of active control arises to more significant than that of semiactive control. One might see that the peak of PDFs of the former approaches to 0.9, while the peak of PDFs of the later approaches to 0.45. As mentioned previously, the semiactive and passive controllers still remain challenges in the displacement control of structures. Besides, the semiactive controller designed as the ratio of coefficients of weighting matrices 8×10^{13} exhibits a worse instead of a better control effectiveness than the active controller design as a smaller ratio of coefficients of weighting matrices 8×10^{12}.

In order to reveal the influence of the semiactive control upon the dynamic performance of MR dampers, Fig. 8.25 shows the relation between the damper force and the damper displacement, damper velocity under a sample of seismic excitation. It is seen that the relation curves between damper velocity and damper force nearly all distribute in the first and third quadrants, indicating that the semiactive control force always remains an opposite direction to the damper velocity. The rationality is thus proposed that the MR damper can change the output timely so as to trace the active optimal control force in real time. The predictive and experimental data as an up-scaled profile of MR damper force curves are shown in Fig. 8.25 as well. In conjunction with the modified Bouc–Wen hysteretic model, the predictive and experimental data are derived from a 3-kN MR damper in type of VersaFlo MRX-135GD

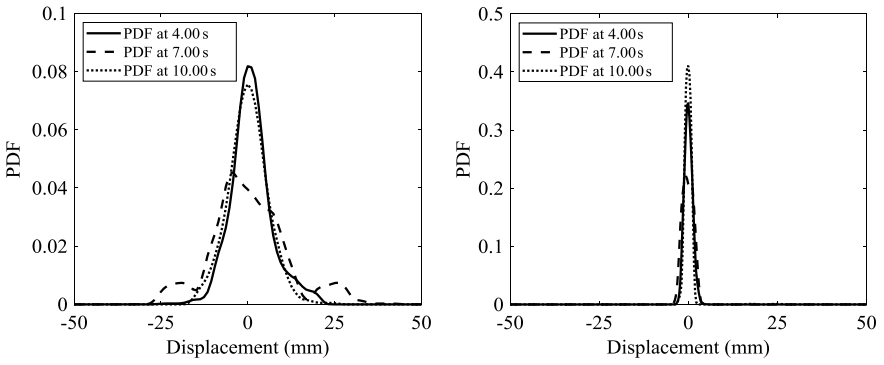

Fig. 8.24 PDFs of interstory drift at typical instants of time with and without MR damping controls

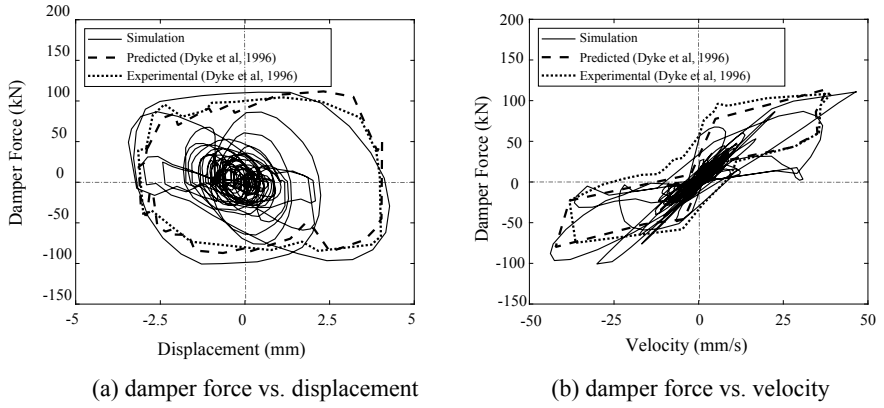

Fig. 8.25 Relation between damper force and damper displacement, damper velocity under the sample of seismic excitation

under a narrowband excitation of white Gaussian noise (Dyke et al. 1996; Spencer et al. 1997). It is revealed that the semiactive control can well accommodate the dynamic performance of MR dampers, which behaves a similarity as the Bouc–Wen hysteretic model with strength deterioration, stiffness degradation, and pinch effect (Wen 1976).

For illustrating the generation of input currents to the MR damper, the shear-valve mode MR damper with double rods in specification of MRD-9000 is employed which has a moderate performance as required by this numerical example. The simulated data of the MR damper under displacement amplitude of 25.4 mm, excitation frequency of 0.5 Hz, and input current of 0.0–2.0 A is utilized. A modified Bouc–Wen hysteretic model is applied to simulate the dynamic performance of the MR damper. Using the parameter identification procedure addressed in Sect. 8.3.2,

the constant parameters of the modified Bouc–Wen hysteretic model for the MRD-9000 are denoted by $[x_0, k_1, c_0, k_0, g, n, b, A] = [0.0, 158.55, 469{,}042.70, 612.79, 98{,}540.12, 2.01, 73{,}224.85, 9{,}253.30]$, and the current variant parameters are denoted by $c_1 = -5.15 \times 10^6 I^2 + 1.73 \times 10^7 I + 3.63 \times 10^6$, $\alpha = -2.42 \times 10^5 I^2 + 8.71 \times 10^5 I + 7.34 \times 10^6$.

According to the parameterized model and the system state of structures, a numerical procedure by virtue of backpropagation (BP) neural network algorithm is employed to generate the current signal loaded on the MR damper. The BP algorithm can be readily implemented in conjunction with the MATLAB toolbox function *nftool*. The numbers of input nodes, output nodes, and implication nodes are 7, 1, and 13, respectively. For solving the differential equations of the Bouc–Wen hysteretic model in the numerical procedure, the four-order Runge–Kutta method is employed here and implemented by the solver *ode4* of MATLAB/Simulink as well.

Prior to the generation of input currents, a step of sample training needs to be proceeded to activate the BP neural network-based retrorse model of MR dampers. A 20-s time series with 1000 data points is used for training and validation, which consists of three segments: white Gaussian noise of current and displacement in the first 10 s, high-amplitude sine current and white Gaussian noise of displacement in the next 5 s, and low-amplitude sine current and white Gaussian noise of displacement in the last 5 s. The validation of sample data shows that the goodness of fit attains to more than 98%. Other three different cases are addressed to verify the effectiveness of the retrorse model of MR dampers, involving Case 1: white Gaussian noise of current and displacement, Case 2: sine current and white Gaussian noise of displacement, and Case 3: constant current and sine displacement. The current and displacement in each case are 20-s time series with 1000 data points. Figure 8.26 shows the expected and identified input currents and the associated outputs of MR dampers in the three cases. It is seen that the identified damper force matches well with the expected, of which the errors of three cases are 3.12%, 6.93%, and 2.54%, respectively.

Similarly, if the system state and the output of MR dampers are known, one can readily derive the input current. In this study, the identification of optimal current for MR damper control of structures under three different samples of seismic ground motions is carried out; see Fig. 8.27. It is seen that the optimal currents used for semiactive control of structures arise to irregularly fluctuate in the range of 0.0–0.6 A, which are significantly different from the samples of seismic ground motions. One might recognize that the real-time feedback control exhibits a practical significance for improving the structural performance; the development of highly efficient MR damper control ought to follow an accurate modality from the present simple Bang–Bang control or Passive-on and Passive-off step controls in practice. It is also noted that the methodology of physically based stochastic optimal control, the probabilistic optimization and design of controller parameters, and control device placement play an important role in this developing process.

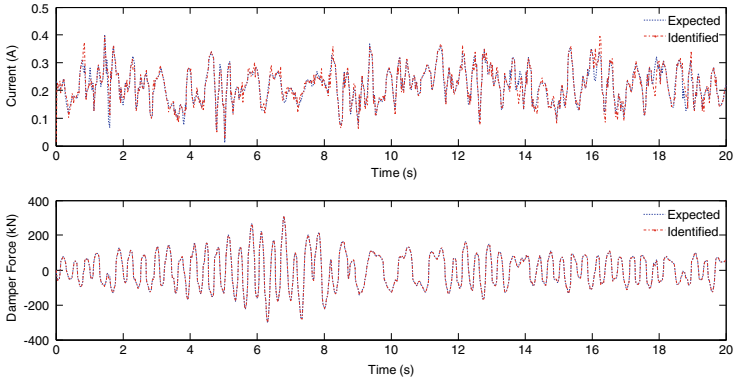

(a) Case 1: White Gaussian noises of current and displacement

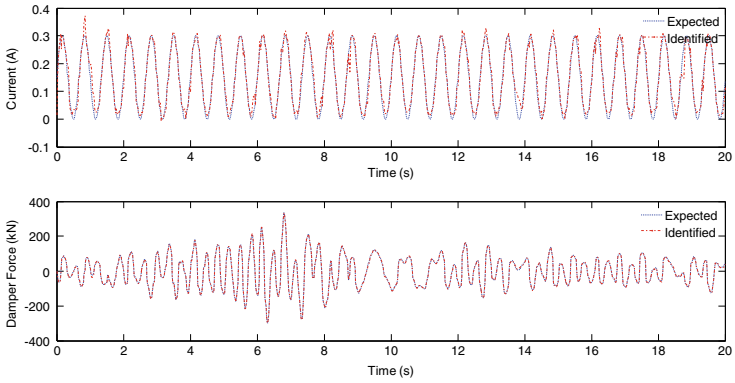

(b) Case 2: sine function of current and Gaussian noise of displacement

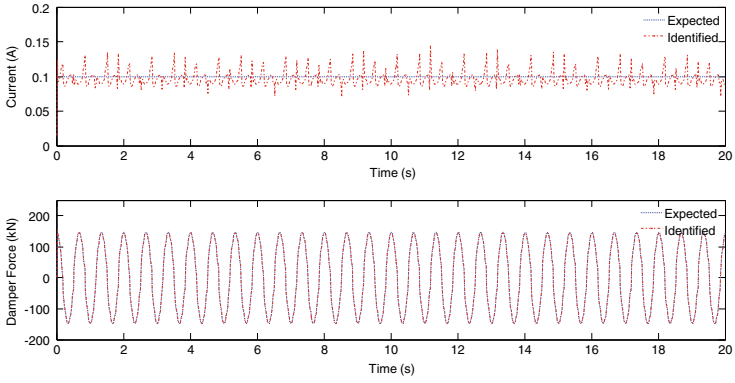

(c) Case 3: Sine function of current and white Gaussian noise of displacement

Fig. 8.26 Expected and identified input currents and associated outputs of MR dampers in three cases

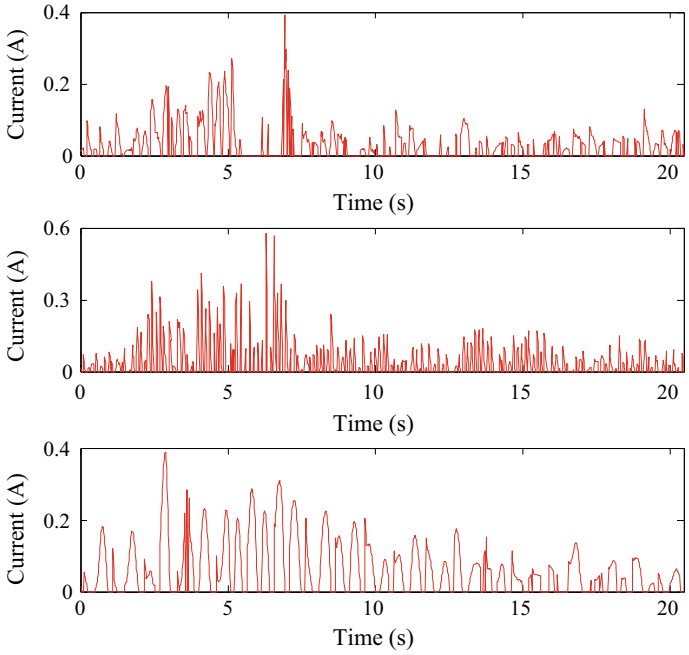

Fig. 8.27 Optimal currents of MR damping control of structure under three different samples of seismic ground motions

8.5 Discussions and Summaries

The input current as the control law of regulating MR dampers is often derived from the inverse solution of damper models. How the dynamic performance of MR dampers can be fulfilled relies upon the effectiveness of the damper model. This chapter first addresses the stochastic optimal control of structures with MR dampers by virtue of bound Hrovat algorithm. In conjunction with the provided MR damper, the dynamic performance and parameterized models of MR dampers under input current, loading frequency, and amplitude of sine displacement are then illustrated. The parameter identification of MR damper model and the influence of input current on the microstructured behaviors of MR suspensions are investigated.

Molecular dynamics simulation reveals the mechanism of microstructured behaviors of MR suspensions in MR dampers, which provides a new perspective for the control law optimization and performance enhancement of MR dampers: using the numerical simulation and experimental analysis to explore the quantitative relationship between suspension structures of MR fluids, input current and material parameters of MR fluids such as dynamic viscosity and yield stress, and to reveal the physical essence of influence of eddy current effect of MR fluids and of nonlinear magnetization of MR suspensions upon the performance of MR dampers. This mul-

tiscale scheme allows for a high-efficient regulation of MR dampers so as to attain the desired performance of controlled structures.

For illustrative purposes, the stochastic optimal control of MR damping system subjected to random seismic ground motion is carried out. As the control criterion of tracing the reference active optimal control force, the parameter design of MR dampers and identification of input current are performed. Numerical results reveal that the appropriately designed semiactive controller can achieve almost the same effectiveness as the active controller; the dynamic performance of MR dampers, meanwhile, exhibits similarities to the Bouc–Wen hysteretic model with the strength deterioration, the stiffness degradation, and the pinch effect.

References

Asai T, Chang CM, Spencer BF Jr (2015) Real-time hybrid simulation of a smart base-isolated building. J Eng Mech 141(3):04014128-1-10

Boada MJL, Calvo JA, Boada BL, Diaz V (2011) Modeling of a magnetorheological damper by recursive lazy learning. Int J Non-Linear Mech 46(3):479–485

Bouc R (1967) Forced vibration of mechanical system with hysteresis. In: Proceedings of 4th conference on nonlinear oscillations, Prague, Czechoslovakia

Carlson JD, Jolly MR (2000) MR fluid, foam and elastomer devices. Mechatronics 10(4–5):555–569

Carrion JE, Spencer BF Jr, Phill BM (2009) Real-time hybrid simulation for structural control performance assessment. Earthq Eng Eng Vibr 8(4):481–492

Casciati F, Magonette G, Marazzi F (2006) The technology of semiactive devices and applications in vibration mitigation. John Wiley & Sons, Ltd

Cha YJ, Zhang JQ, Agrawal AK, Dong BP, Friedman A, Dyke SJ, Ricles J (2013) Comparative studies of semiactive control strategies for MR dampers: pure simulation and real-time hybrid tests. J Struct Eng 139(7):1237–1248

Chae Y, Ricles JM, Sause R (2013) Modeling of a large-scale magneto-rheological damper for seismic hazard mitigation. Part II: semi-active mode. Earthq Eng Struct Dyn 42(5):687–703

Chang CC, Roschke P (1998) Neural network modeling of a magnetorheological damper. J Intell Mater Syst Struct 9(9):755–764

Charalampakis AE, Koumousis VK (2008) Identification of Bouc-Wen hysteretic systems by a hybrid evolutionary algorithm. J Sound Vib 314(3–5):571–585

Chu SY, Soong TT, Reinhorn AM (2005) Active, hybrid and semi-active structural control. Wiley, New York

Dan M, Ishizawa Y, Tanaka S, Nakahara S, Wakayama S, Kohiyama M (2015) Vibration characteristics change of a base-isolated building with semi-active dampers before, during, and after the 2011 Great East Japan earthquake. Earthq Struct 8(4):889–913

Dyke SJ, Spencer BF Jr, Sain MK, Carlson JD (1996) Modeling and control of magnetorheological dampers for seismic response reduction. Smart Mater Struct 5:565–575

Dyke SJ, Spencer BF Jr, Sain MK, Carlson JD (1998) An experimental study of MR dampers for seismic protection. Smart Mater Struct 7(5):693–703

Hogsberg J (2011) The role of negative stiffness in semi-active control of magneto-rheological dampers. Struct Control Health Monit 18(3):289–304

Hrovat D, Barak P, Rabins M (1983) Semi-active versus passive or active tuned mass dampers for structural control. ASCE J Eng Mech 109(3):691–705

Ikhouane F, Rodellar J (2005) On the hysteretic Bouc-Wen model. Nonlinear Dyn 42(1):63–78

Imaduddin F, Mazlan SA, Zamzuri H (2013) A design and modelling review of rotary magnetorheological damper. Mater Des 51:575–591

Jansen LM, Dyke SJ (2000) Semi-active control strategies for MR dampers comparative study. ASCE J Eng Mech 126(8):795–803
Jung HJ, Jang DD, Lee HJ, Lee IW, Cho SW (2010) Feasibility test of adaptive passive control system using MR fluid damper with electromagnetic induction part. J Eng Mech 136(2):254–259
Li J, Chen JB, Fan WL (2007) The equivalent extreme-value event and evaluation of the structural system reliability. Struct Saf 29(2):112–131
Liu WK, Karpov EG, Park HS (2006) Nano mechanics and materials: theory, multiscale methods and applications. Wiley, New York
Metered H, Bonello P, Oyadiji SO (2010) The experimental identification of magnetorheological dampers and evaluation of their controllers. Mech Syst Signal Process 24(4):976–994
Nagarajaiah S, Narasimhan S (2006) Smart base-isolated benchmark building. Part II: phase I sample controllers for linear isolation systems. Struct Control Health Monit 13(2–3):589–604
Ni YQ, Chen Y, Ko JM, Cao DQ (2002) Neuro-control of cable vibration using semi-active magneto-rheological dampers. Eng Struct 24:295–307
Patten WN, Mo C, Kuehn J, Lee J (1998) A primer on design of semi-active vibration absorbers (SAVA). ASCE J Eng Mech 124(1):61–68
Peng YB, Li J (2011) Multiscale analysis of stochastic fluctuation of dynamic yield of magnetorheological fluids. Int J Multiscale Comput Eng 9(2):175–191
Peng YB, Ghanem R, Li J (2012) Investigations of microstructured behaviors of magnetorheological suspensions. J Intell Mater Syst Struct 23(12):1349–1368
Peng YB, Yang JG, Li J (2017) Seismic risk based stochastic optimal control of structures using magnetorheological dampers. Nat Hazards Rev ASCE 18(1):UNSP B4016001
Peng YB, Yang JG, Li J (2018) Parameter identification of modified Bouc-Wen model and analysis of size effect of magnetorheological dampers. J Intell Mater Syst Struct 29(7):1464–1480
Plimpton SJ (1995) Fast parallel algorithms for short-range molecular dynamics. J Comput Phys 117:1–19. lammps.sandia.gov
Soong TT (1990) Active structural control: theory and practice. Longman Scientific & Technical, New York
Spencer BF Jr, Sain MK, Carlson JD (1997) Phenomenological model of magnetorheological damper. ASCE J Eng Mech 123(3):230–238
Swope WC, Andersen HC, Berens PH, Wilson KR (1982) A computer simulation method for the calculation of equilibrium constrains for the formation of physical cluster of molecules: application to small water clusters. J Chem Phys 76(1):637–649
Tsang HH, Su RKL, Chandler AM (2006) Simplified inverse dynamics models for MR fluid dampers. Eng Struct 28(3):327–341
Tse T, Chang CC (2004) Shear-mode rotary magnetorheological damper for small-scale structural control experiments. J Struct Eng 130(6):904–911
Verlet L (1967) Computer "experiments" on classical fluids I: thermodynamical properties of Lennard-Jones molecules. Phys Rev 159(1):98–103
Wang YM, Dyke S (2013) Modal-based LQG for smart base isolation system design in seismic response control. Struct Control Health Monit 20(5):753–768
Wen YK (1976) Method for random vibration of hysteretic systems. ASCE J Eng Mech Div 102(2):249–263
Xu ZD, Guo YQ (2008) Neuro-fuzzy control strategy for earthquake-excited nonlinear magnetorheological structures. Soil Dyn Earthq Eng 28(9):717–727
Xu ZD, Jia DH, Zhang XC (2012) Performance tests and mathematical model considering magnetic saturation for magnetorheological damper. J Intell Mater Syst Struct 23(12):1331–1349
Yang G (2001) Large-scale magnetorheological fluid damper for vibration mitigation: modeling, testing and control. PhD Thesis, University of Notre Dame, USA
Yang G, Spencer BF Jr, Carlson JD, Sain MK (2002) Large-scale MR fluid dampers: modeling and dynamic performance considerations. Eng Struct 24(3):309–323
Yang MG, Li CY, Chen ZQ (2013) A new simple non-linear hysteretic model for MR damper and verification of seismic response reduction experiment. Eng Struct 52:434–445

Ying ZG, Ni YQ, Ko JM (2009) A semi-active stochastic optimal control strategy for nonlinear structural systems with MR dampers. Smart Struct Syst 5(1):69–79

Yoshioka H, Ramallo JC, Spencer BF Jr (2002) "Smart" base isolation strategies employing magnetorheological dampers. J Eng Mech 128(5):540–551

Zhong WX (2004) On precise integration method. J Comput Appl Math 163:59–78